Tuning the selectivity of visible light-driven hydroxylation of benzene to phenol by using Cu, Fe and V oxides supported on N-doped TiO_2

Antonietta Mancuso[1], Alessandro Gottuso[2], Francesco Parrino[2*], Rosaria Anna Picca[4], Vincenzo Venditto[3], Olga Sacco[3*] and Vincenzo Vaiano[1]

[1] Department of Industrial Engineering, University of Salerno, Via Giovanni Paolo II 132, 84084 Fisciano (SA), Italy

[2] Department of Industrial Engineering, University of Trento, Via Sommarive 9, 30123 Trento (TN), Italy

[3] Department of Chemistry and Biology "A. Zambelli" and INSTM Research Unit, University of Salerno, Via Giovanni Paolo II, 132, 84084 Fisciano (SA), Italy

[4] Department of Chemistry, University of Bari Aldo Moro, Via E. Orabona 4, 70125 Bari (BA), Italy

*Corresponding authors:

E-mail: francesco.parrino@unitn.it (Francesco Parrino); osacco@unisa.it (Olga Sacco)

Abstract

Cu, Fe and V oxides supported on N-TiO_2 (Cu/N-TiO_2, Fe/N-TiO_2, and V/N-TiO_2) were synthetized by incipient wet impregnation method. The prepared photocatalysts were analyzed by N_2 adsorption at -196°C to measure the specific surface area (S_{BET}) values, scanning electron microscopy (SEM), wide-angle X-ray diffraction (WAXD), X-ray photoelectron spectroscopy (XPS), Raman, photoluminescence and ultraviolet-visible diffuse reflectance (UV-vis DRS)

spectroscopies. The prepared photocatalysts were tested in the hydroxylation of benzene to phenol under visible light irradiation in the presence of H_2O_2 as the oxidant. After 360 min of irradiation, Cu/N-TiO_2 achieves a phenol yield equal to 25%, significantly higher than that observed with Fe/N-TiO_2 (2%) and V/N-TiO_2 (2.5%). Moreover, Cu/N-TiO_2 photocatalyst exhibited a phenol yield higher than that reported in the literature dealing with TiO_2 based photocatalysts for photocatalytic benzene hydroxylation. The better photoactivity of Cu/N-TiO_2 in phenol production was justified by considering both electronic and surface photocatalyst features. In detail, a significant optical absorption in the visible region has been highlighted, due to the intense electronic interactions between CuO and N-TiO_2. Moreover, the surface of the copper oxide component shows low affinity with phenol molecules. Therefore, once photocatalytically generated, phenol easily desorbs from the Cu/N-TiO_2 surface thus limiting parasitic overoxidation reactions. In fact, after 180 min of visible light irradiation, only 30% of phenol was degraded by Cu/N-TiO_2, while 100% and 81% of it was degraded by Fe/N-TiO_2 and V/N-TiO_2, respectively. From the comparison of phenol production kinetic constants, obtained by fitting the experimental data with the least-squares methods, showed that the highest rate of phenol formation ($k=1.41\cdot10^{-3}$ min^{-1}) was obtained by using the Cu/N-TiO_2 photocatalyst. Cu/N-TiO_2 has been recovered from the aqueous solution after a photocatalytic run and reused four times with no reduction in benzene conversion and phenol yield, thus confirming the high stability of the catalytic system.

Keywords: CuO; N-TiO_2; visible light photocatalysis; hydroxylation; phenol; benzene.

1. Introduction

Phenol is currently produced through the 3-steps cumene process, which starts from benzene, and suffers drawbacks such as high energy consumption, low yields (ca. 5%), dangerous intermediates, such as cumene hydroperoxide, and the generation of acetone as a by-product, which strongly limits the market price [1-3]. Therefore, the direct hydroxylation of benzene would be a greener alternative to produce phenol, not only to reduce the hazardous nature of the cumene process, but also in terms of mass economy [4]. Heterogeneous photocatalysis is recognized as an innovative and green technology because it can be carried out under mild operating conditions, and in the presence of cheap and non-toxic semiconductors acting as photocatalysts activable by solar or artificial light with low-energy consumption [5]. The majority of photocatalytic processes, both for the degradation of organic compounds and for the synthesis of organic products, are based on photoinduced charge transfer, which occurs at the interface of the semiconductor, being the photogenerated electrons and holes, respectively, primary reducing and oxidizing agents [6-8]. Photocatalytic reactions are commonly performed under UV light [9], but suitable photocatalytic systems can also be activated by low-energy visible light, making available a powerful and sustainable route for organic synthesis and the production of valuable chemical compounds [10]. However, photocatalysis also presents some drawbacks, such as the low selectivity towards the partial oxidation products, especially by using water as the solvent [5, 11]. In the field of chemical reactions, it is certainly of research interest to find strategies to perform organic syntheses in a single step, and to control the reaction path in order to improve the selectivity towards the desired product, assuring its separation and recovery. The photocatalytic hydroxylation of benzene to phenol is an interesting example of green organic synthesis. Phenol is a chemical widely used as a disinfectant and as a precursor for the production

of resins and pharmaceutical products. However, the application of photocatalytic benzene hydroxylation at an industrial level is limited by its fast kinetics, which makes the process highly non-selective.

This problem has been successfully faced by coupling photocatalysis with a membrane separation unit [12]. In general, this combined approach is useful for many other photocatalytic organic syntheses of high-added value compounds [13] as it allows to separate the target compound from the reacting mixture. However, the optimization of the intrinsic photocatalyst features remains a necessary step, in order to design effective processes capable of competing with existing industrial processes. In detail, the modification of the physical and chemical properties of the photocatalysts, for example by coupling together different semiconductors, could be a possible strategy to improve the efficiency and selectivity of the photocatalytic oxidation of benzene [5]. Each photocatalyst must be optimized and selected for specific organic synthesis reactions since the selectivity control depends on the molecular structure and properties of the organic substrate and its specific interaction with the photocatalyst. In-depth studies are required to unveil the relationship between the surface properties of the catalyst and substrate molecules and to be able to control the typical overoxidation that occurs during photohydroxylation of aromatic compounds, such as benzene. In detail, Park and Choi studied the photocatalytic conversion of benzene into phenol and showed the possibility of increasing the phenol yield and selectivity by adding Fe^{3+} or/and H_2O_2 to the TiO_2 suspension or by modifying the surface of the catalyst by deposition of Pt nanoparticles [14]. Ide et al. formulated a layered titanate photocatalyst decorated with gold nanoparticles, which catalyzed the oxidation of aqueous benzene to phenol under visible light irradiation. Moreover, it was found that the reaction efficiency was improved when the oxidation was performed with the addition of phenol into the

92 starting mixture, by leading to an appreciable increase in yield and selectivity [15]. Devaraji et al.
93 demonstrated that the introduction of vanadium into the TiO_2 lattice, and the photodeposition of
94 gold on the photocatalytic surface increased the benzene conversion and selectivity to phenol [16].
95 The liquid-phase hydroxylation of benzene to phenol was also investigated by Tanarungsun et al. in
96 the presence of transition metals (copper, vanadium, iron) impregnated on a TiO_2 support,
97 demonstrating a higher phenol yield obtained with the impregnated TiO_2 systems under UV light
98 compared to bare TiO_2 [17]. Based on the results reported in the literature and considering our
99 preliminary results on N-doped TiO_2 photocatalyst [18], in this work transition metal oxides (iron,
100 vanadium and copper oxide) were supported on N-TiO_2 and tested in the hydroxylation of benzene
101 to phenol under visible light.
102
103 ## 2. Materials and methods
104 ### 2.1 Chemicals and reagents
105 Benzene (purity>99.7%) and cyclohexane (purity>99%) were purchased from Sigma Aldrich.
106 Distilled water and acetonitrile (purity>99.9%) were acquired from Carlo Erba. Hydrogen peroxide
107 solution used as oxidant was purchased from Sigma Aldrich (30 wt%). Titanium(IV) isopropoxide
108 (purity>97%), copper nitrate trihydrate, iron nitrate nonahydrate and ammonium metavanadate
109 were provided by Sigma Aldrich.
110
111 ### 2.2 N-doped TiO_2 preparation
112 N-doped TiO_2 (N-TiO_2) photocatalyst was synthesized by sol-gel method using ammonia solution
113 (30 wt%), as nitrogen source, and titanium isopropoxide. The preparation was carried out according

to the procedure reported by Sacco et al. [19]. Briefly, the synthesis of N-TiO_2 was carried out at 0 °C until the formation of a precipitate, which washed using distilled water and finally calcined at 450°C for 30 min. The N/Ti nominal molar ratio used in the photocatalyst preparation was equal to 18.6 [19].

2.3 Preparation of transition metal oxides loaded on N-TiO_2 photocatalyst

Cu, Fe and V oxides loaded on N-TiO_2 (named Cu/N-TiO_2, Fe/N-TiO_2, and V/N-TiO_2) were prepared by the incipient wet impregnation method [20]. 1 g of N-TiO_2 powder was suspended in 100 mL of aqueous solutions containing the appropriate amount of trihydrate copper nitrate (0.23 g), nonahydrate iron nitrate (0.38 g) or ammonium metavanadate (0.11 g) in order to obtain photocatalysts with a loading of each metal equal to 5 wt%, as considered in literature [17]. The suspensions were dried at 120°C for 12 h and the obtained powders were finally calcined in a muffle oven at 450°C for 30 min.

2.4 Photocatalyst characterization techniques

Wide-angle X-ray diffraction (WAXD) patterns were obtained with an automatic Bruker D8 Advance diffractometer (VANTEC-1 detector) using reflection geometry and nickel filtered Cu-Kα radiation. The average crystallite size of the synthesized powders was calculated using the Scherrer equation [21]. The Brunauer-Emmett-Teller (BET) surface area of the samples was measured from dynamic N_2 adsorption measurement at -196 °C, performed by a Costech Sorptometer 1042 after a pre-treatment for 30 min in He flow at 150 °C.

Laser Raman spectra were attained at room temperature with a Dispersive MicroRaman (Invia, Renishaw), equipped with 514 nm laser, in the range 100 - 2000 cm^{-1} Raman shift.

The ultraviolet-visible diffuse reflectance spectra (UV-Vis DRS) of the samples were obtained using a Perkin Elmer spectrometer Lambda 35 spectrophotometer equipped with a RSA-PE-20 reflectance spectroscopy accessory (Labsphere Inc., North Sutton, NH). The indirect band gap values of samples were obtained through the corresponding Kubelka–Munk function ($F(R_\infty)$) and by plotting $[F(R_\infty)\cdot h\nu]^{1/2}$ vs $h\nu$ (eV) [22, 23].

X-ray photoelectron spectroscopy (XPS) characterization of the catalysts' surface was performed on a PHI Versaprobe II spectrometer using monochromatized Al-Kα source (47.6 W) at constant charge neutralization with a 200 μm spot size. Spectra were acquired on at least three points of the samples and processed with ULVAC-PHI MultiPak® (v. 9.9.3) software. The Binding Energy (BE) scale was calibrated setting the aliphatic component of C1s at 284.8 eV. Energy pass was set at 46.95 eV for high-resolution (HR) spectra.

Fluorescence spectra of the powders were recorded by suspending them in cyclohexane and by using a Jasco FP-6300 spectrofluorimeter (Jasco, Tokyo, Japan) with λ= 325 nm as the excitation wavelength. Field emission scanning electron microscopy (FE-SEM) analysis was carried out by means of FE-SEM, Supra 40/40VP equipped with an EDAX probe (Zeiss, Oberkochen, Germany), operating at a voltage of 20 kV on specimens where a 6 nm thin layer of Pt/Pd had been deposited under Ar atmosphere.

157 **2.5 Photocatalytic activity tests**

158 The benzene hydroxylation reaction was performed in 200 mL aqueous solution containing benzene
159 (initial concentration: 25.6 mmol/L) and acetonitrile (2.3 mL) as a co-solvent with 0.15 g/L of
160 Cu/N-TiO_2, Fe/N-TiO_2, and V/N-TiO_2 photocatalyst under continuous stirring in a cylindrical Pyrex
161 photoreactor. 2.8 mL of H_2O_2 (30 wt% in H_2O) were added to the reaction mixture (H_2O_2
162 concentration: 136 mmol/L).
163 The system was first kept under dark for 60 min at room temperature, to reach the adsorption-
164 desorption equilibrium of benzene. Then, the reactor was irradiated for 600 min by a LEDs strip
165 emitting visible light (emission range: 400–800 nm; irradiance: 16 W/m^2) placed around and in
166 contact to the external surface of the Pyrex reactor. A fan cooled down the reactor during irradiation
167 time. Solution aliquots were withdrawn from the reactor at different times by a 1 mL syringe,
168 filtered through a 0.22 μm CA filter (SIMPLEPURE) to remove solid particles, and immediately
169 analyzed quantitatively by an Agilent gas chromatograph (model 7820 A) equipped with a flame
170 ionization detector (FID) to evaluate the benzene and phenol concentration. Some photocatalytic
171 tests were carried out using 100 mL of phenol (initial concentration: 0.53 mmol/L) aqueous
172 solution, 0.15 g/L of photocatalyst and H_2O_2 concentration equal to 136 mmol/L. GC separation
173 was achieved with a DB Heavy Wax fused-silica capillary column (30m x 0.35mm i.d. x 0.25μm
174 stationary phase thickness) under the following conditions: column temperature 40-300°C (40°C
175 held 2 min, rate 5°C/min to 90°C, rate 20°C/min to 250°C, held 10 min); helium at a constant flow
176 rate of 1 mL/min; injection port operated at 10:1 split mode; the temperature of injector and detector
177 at 180°C and 300°C, respectively. Hydroquinone, resorcinol, p-benzoquinone and catechol were
178 determined quantitatively by HPLC, using a Dionex UltiMate 3000 Thermo Scientific system

equipped with DAD detector, column thermostat and automatic sample injector with 100µL loop. Separations were carried out on a Phenomenex Luna C-18 column (150 x 4.6 mm i.d.; 5µm) eluted with a mixture of water (solvent A) and acetonitrile (solvent B) according to the program: 0-14 min, 15% B (isocratic); 14-23 min, 60-100% B (linear gradient); 23-30 min, 15% B (isocratic). The chromatographic conditions were: oven temperature 35°C; flow rate 0.8 mL/min; injection volume 50 µL and UV detector at 270 nm. Benzene conversion (Bz_{conv}), yield (Y_P) and selectivity (S_P) towards phenol and by-products were evaluated according to Eqs. 1-3.

$$benzene\ conversion\ (Bz_{conv}) = \left(1 - \frac{C}{C_0}\right) x\ 100 \quad (1)$$

$$yield\ to\ P\ (Y_P) = \left(\frac{S}{Q_0}\right) x\ 100 \quad (2)$$

$$selectivity\ to\ P\ (S_P)\ = \left(\frac{S\ (or\ Deg)}{S_{TOT}\ + Deg}\right) x\ 100 \quad (3)$$

Where:

C_0 = benzene concentration after the dark period (mmol/L);

C = benzene concentration at the generic irradiation time (mmol/L);

Q_0 = moles of benzene in solution after the dark period (mmol);

P = reaction product (phenol or hydroquinone or catechol or resorcinol or p-benzoquinone);

S_{TOT} = total moles of the reaction products in liquid phase detected by HPLC (mmol);

S = moles of phenol or hydroquinone or catechol or resorcinol or p-benzoquinone in liquid phase (mmol);

D_{eg}= ring-opened products and CO_2 = (benzene reacted−S_{TOT}) [24].

3. Results and discussion

3.1 Photocatalysts characterization results

FE-SEM images of the Cu, Fe and V oxides supported on N-TiO_2 samples are shown in Figure 1, along with Cu, Fe and V atoms EDX maps.

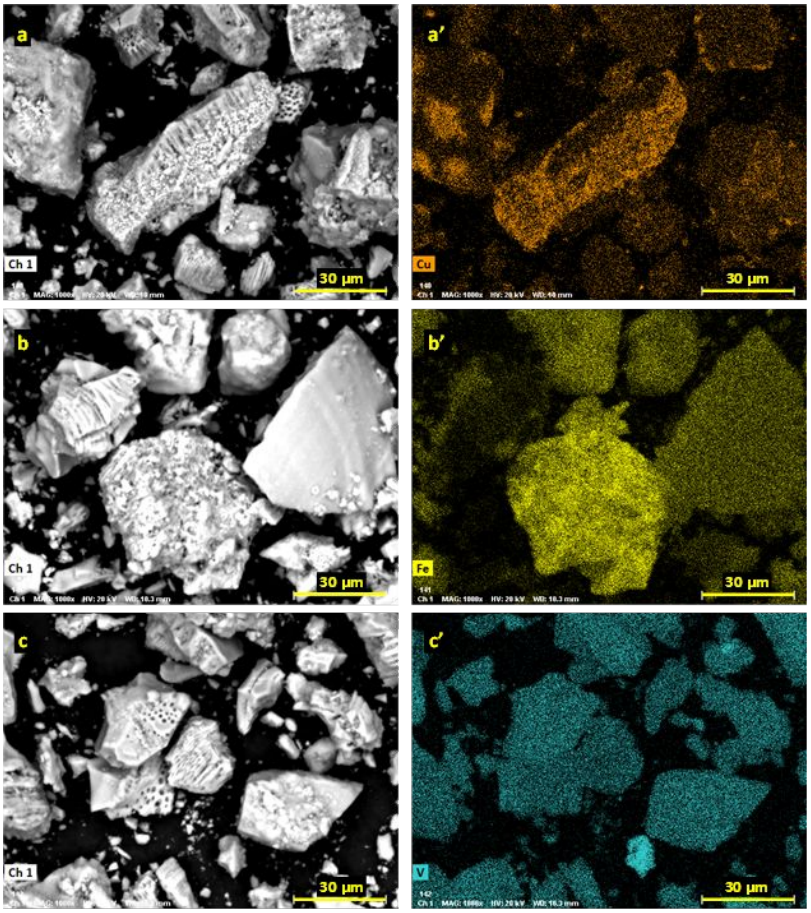

Figure 1. SEM images of Cu/N-TiO_2 (a), Fe/N-TiO_2 (b), and V/N-TiO_2 (c) samples along with the correspondent Cu (a'), Fe (b'), and V (c') atoms maps.

208 The three mixed oxide catalytic systems show a similar micrometric aggregate morphology. Cu, Fe
209 and V atoms are homogeneously distributed throughout the samples and their normalized atomic
210 weight percent is 5.9, 5.5 and 3.3%, respectively.
211 The crystalline phase structure of all the samples was identified by wide-angle X-ray diffraction
212 (WAXD) (Figure 2). The WAXD patterns of all the synthesized samples showed the typical signals
213 of TiO_2 anatase crystalline phase [25]. The peaks were located at the 2θ values of 25.3, 37.8, 48.1,
214 53.9, 55.1, 63.1 and 69.2° and they correspond to (101), (004), (200), (105), (211), (204) and (116)
215 anatase lattice planes [26]. However, the diffraction pattern of the N-TiO_2 sample evidenced a weak
216 diffraction peak at 27° that could be attributed to the presence of TiO_2 in the rutile crystalline phase
217 [27]. The peak at 38° related to Fe_2O_3 is not revealed for Fe/N-TiO_2 as also reported in the literature
218 for similar systems [17], probably because the loading of Fe (nominally 5% wt) is below the detection
219 limit of the instrument. A similar result was obtained for V/N-TiO_2. Also in this case, the absence of
220 further peaks belonging to the V_2O_5 orthorhombic phase is probably due to the low vanadium
221 loading. Conversely, the presence of peaks at 2θ = 35.2, 36.2 and 38.3°, corresponding to (110),
222 (002) and (111) CuO lattice planes (inset in Figure 2) [28, 29], is detected for the Cu/N-TiO_2 sample.
223

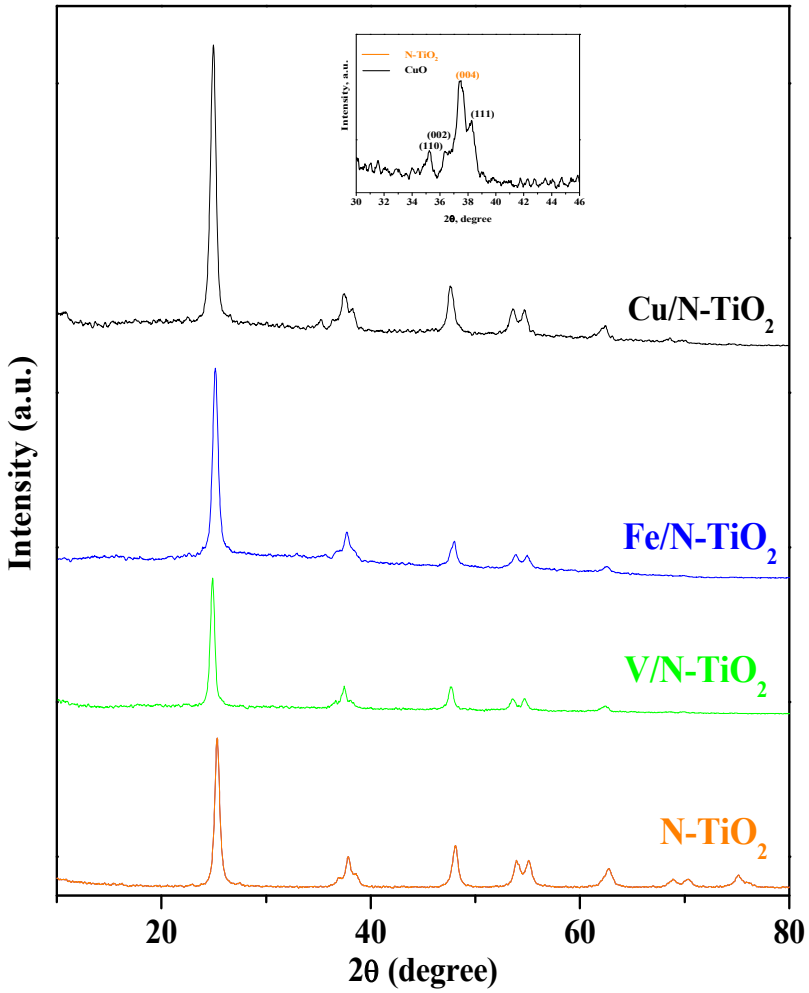

Figure 2. Wide angle X-ray diffraction (WAXD) patterns of N-TiO_2, Cu/N-TiO_2, Fe/N-TiO_2 and V/N-TiO_2 samples.

The Raman spectra of N-TiO_2, Cu/N-TiO_2, Fe/N-TiO_2 and V/N-TiO_2 samples are shown in Figure 3.

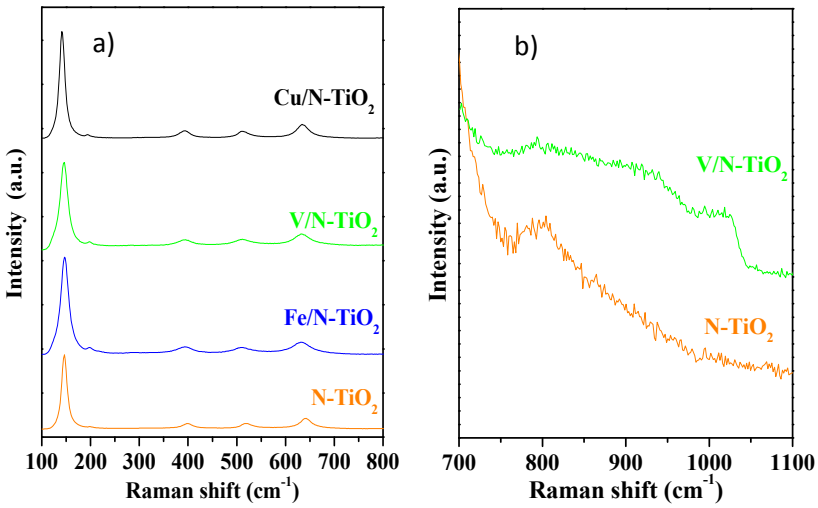

Figure 3. Raman spectra of N-TiO_2, Cu/N-TiO_2, Fe/N-TiO_2 and V/N-TiO_2 (a). Raman spectra of N-TiO_2 and V/N-TiO_2 in narrow Raman shift range 700-1100 cm^{-1}(b).

N-TiO_2 sample showed bands at 144, 397, 516 and 638 cm^{-1} and a weak shoulder at 195 cm^{-1}, due to the Raman-active fundamental modes of anatase [30]. Raman bands associated with CuO and Cu_2O, reported in literature at 279 and 216 cm^{-1}, respectively, were not observed [28, 31].

The Raman spectrum for the Fe/N-TiO_2 sample did not evidence bands related to iron oxides, such as Fe_3O_4 [32]. Conversely, Raman spectrum of V/N-TiO_2 in the narrow range 700-1100 cm^{-1} (Figure 2b) displayed a wide and not very intense band at about 940 cm^{-1}, assigned to the V-O-V functionality, indicating the presence of polyvanadate species. Furthermore, a Raman contribution to about 1016 cm^{-1} was observed for V/N-TiO_2 due to V-O-Ti functionality still assigned to polyvanadate dispersed on N-TiO_2 surface [33].

XPS analysis provided the surface chemical composition of N-TiO_2 and Cu, Fe and V oxides supported on N-TiO_2, as reported in Table 1. N-doping level in all mixed oxide catalytic systems was not affected by the surface deposition process being similar to the value obtained on pristine N-TiO_2 sample.

Table 1. Typical surface chemical composition in terms of atomic % of the as-prepared samples. Values are expressed as the mean ± 1SD on three analysis points. M is the corresponding metal of Cu, Fe and V oxides.

Catalyst	C%	O%	Ti%	N%	M%
N-TiO_2	16.9±1.2	58.2±1.4	24.3±1.5	0.6±0.2	/
Cu/N-TiO_2	19.0±1.3	53.8±1.1	21.0±0.8	0.8±0.3	5.4±0.7
Fe/N-TiO_2	17.3±1.5	56.0±1.5	20.2±0.7	0.6±0.2	5.9±1.1
V/N-TiO_2	21.3±1.4	54.7±1.3	19.3±1.1	0.7±0.2	4.0±0.5

Peak position for $Ti2p_{3/2}$ was found at 458.7±0.1 eV, compatible with TiO_2 [34] (Figure S1 in Supplementary Material). In general, oxide surface deposition processes seemed successful considering the metal percentage on the surface. Analysis of $Cu2p_{3/2}$ HR region has shown that copper is mainly present as Cu(I) (BE = 932.6±0.2 eV) and only 0.5% is ascribable to Cu(II) (BE = 934.5±0.2 eV) (Figure 4a) [34]. $V2p_{3/2}$ component in V2p region (Figure 4b) was fitted with a minor peak at BE = 515.9±0.2 eV, typical of V^{3+}/V^{4+}, and the main at BE = 517.0±0.2 eV attributed to V_2O_5 indicating the possible presence of polyvanadates [35]. Fe speciation by XPS analysis is more difficult though $Fe2p_{3/2}$ position at about 710.7 eV is compatible with Fe(III) species (such as Fe_2O_3 or FeOOH), similar to other reported photocatalysts [36, 37], but the presence of Fe(II) cannot be excluded (Figure S2 in Supplementary Material).

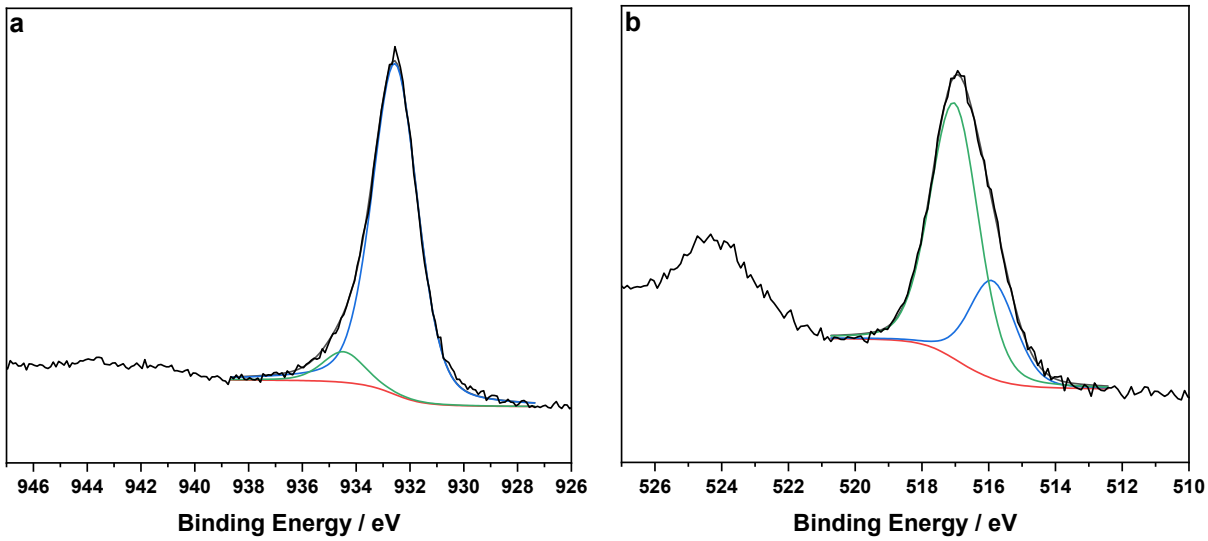

Figure 4. Typical $Cu2p_{3/2}$ spectrum relevant to Cu/N-TiO_2 samples (a); V2p region relevant to V/N-TiO_2 powders (b).

The fluorescence spectra of all the photocatalysts are reported in Figure 5.

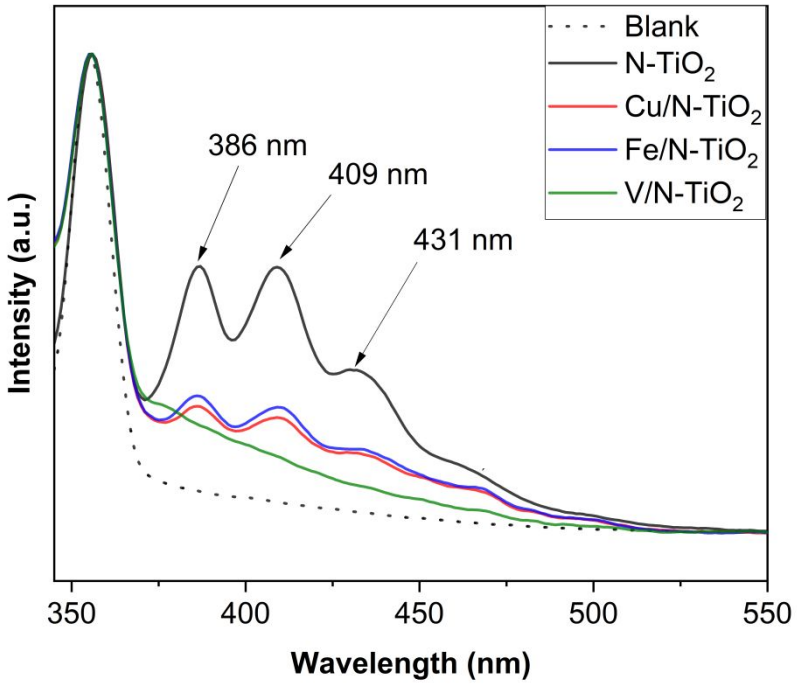

Figure 5. Fluorescence spectra of N-TiO_2 (black line), Cu/N-TiO_2 (red line), Fe/N-TiO_2 (blue line), and V/N-TiO_2 (green line) samples dispersed in cyclohexane. The dashed spectrum is the signal acquired in the presence of neat cyclohexane. All of the spectra have been normalized with respect to this signal. Excitation wavelength: 325 nm.

N-TiO_2 sample shows a broad emission band with well-resolved emission features centered at 386, 409, and 431 nm. The signal at 386 nm has been assigned to band-to-band recombination of TiO_2 anatase phase [38, 39]. Peaks at 409 and 431 nm can be assigned to emission originating from intra-band gap energy states related to oxygen vacancies or nitrogen sites, according to the relevant literature [40-42]. Notably, the signal at 409 nm is also consistent with band-to-band emission of TiO_2 rutile phase [43], which is present in traces according to WAXD analysis. All of the mixed oxide catalytic systems show lower emission with respect to N-TiO_2 sample, thus indicating lower charge recombination possibly due to interfacial electron transfer between the component oxides, resulting in improved spatial charge separation and longer lifetime of the photogenerated charges [44-46].

The BET specific surface area (S_{BET}) and the anatase average crystallite size of the samples (calculated by using the Scherrer equation) are reported in Table 2. Cu/N-TiO_2 and Fe/N-TiO_2 showed an S_{BET} lower than that of the N-TiO_2 sample. This result is in agreement with the higher crystallite size of these two samples with respect to the value observed for the N-TiO_2 photocatalyst.

The optical properties of the photocatalysts have been investigated by evaluating their band gap energy according to the Kubelka-Munk theory, assuming that they are indirect semiconductors. In order to highlight the extent of the electronic interaction between the component oxides, the same analysis has been carried out on mechanical mixtures of the oxides by using the same weight percent of the synthesized powders. Results are reported in Figure 6.

Firstly, it is worth mentioning that the N-TiO_2 sample exhibits improved optical properties in the visible region (Figure 6) with a reduction of band-gap value (E_{bg}) from 3.20 eV (the typical band-gap of undoped TiO_2) [47] to 2.25 eV (Table 2). The narrow band-gap value of N-TiO_2 is attributed to the presence of nitrogen in the TiO_2 lattice [19]. The synthesized mixed oxide catalytic systems show E_{bg} values lower than N-TiO_2 (Table 2) due to the contribution of the transition metal oxides (both band-to-band and d-d transitions occurring in the visible light range) loaded onto the N-TiO_2 sample. By comparing the Tauc plots of the synthesized mixed oxide samples with those of the mechanical mixtures, it is possible to observe a red shift of the absorption edge for all of the synthesized mixed oxide samples, which is particularly relevant for the Cu/N-TiO_2 one.

This behavior has been already reported in the relevant literature for strongly interacting electronic systems, in which an extended alteration of the electronic structure of the mixed phase with respect to the components can be observed. This is reported for instance in vanadium, chromium, iron or nickel-doped TiO_2 prepared by ion implantation [48], for GaN–ZnO solid solutions [49], and for mixed ZnO-Fe_2O_3 photocatalysts [50].

The red shift observed in the synthesized mixed oxide samples with respect to the mechanical mixtures may due to a strong interaction between N-TiO_2 and the oxides dispersed on its surface. In particular, for TiO_2–Fe_2O_3 systems the effective mixing between the surface Fe^{3+} and O2p levels, due to the Ti–O–Fe interfacial bond yielding surface sub-bands, has been reported [51]. A similar mechanism can be inferred in the case of V/N-TiO_2 and Cu/N-TiO_2 samples. However, in the Cu/N-TiO_2 case the red shift of the absorption edge is ca. three times higher with respect to the other samples, thus indicating a stronger electronic interaction between the component oxides, and an improved visible light absorption capability.

Table 2. Crystallite size, specific surface area (S_{BET}), and band gap (E_{bg}) of all of the prepared samples.

Catalyst	Crystallite size (nm)	E_{bg} (eV)indirect	S_{BET} (m^2/g)
N-TiO_2	16	2.25*	30
Cu/N-TiO_2	9	2.00	34
Fe/N-TiO_2	10	2.10	42
V/N-TiO_2	10	2.30	30

* 23

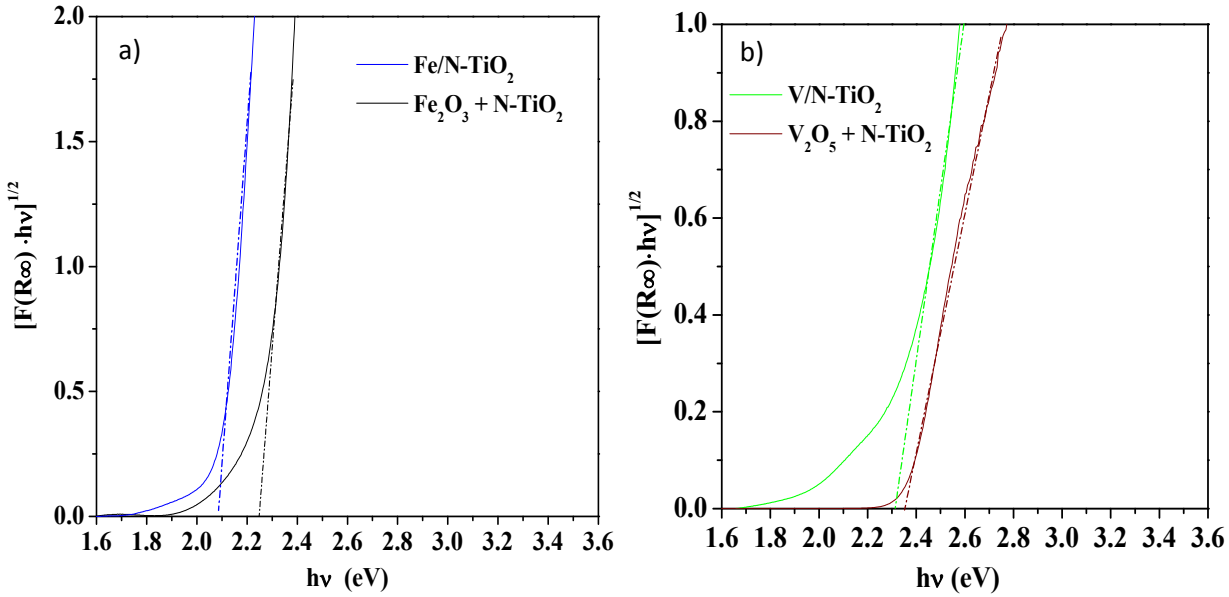

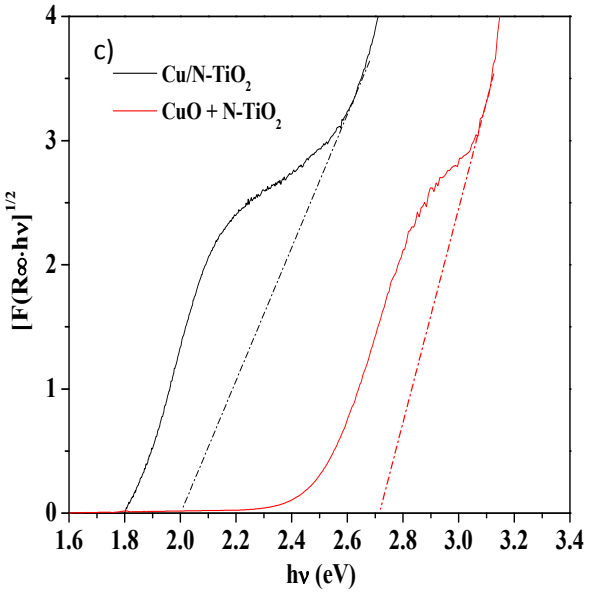

Figure 6. Tauc plots of Fe/N-TiO_2 (blue line), mechanical mixture Fe_2O_3 + N-TiO_2 (grey line) (a), V/N-TiO_2 (green line), mechanical mixture V_2O_5 + N-TiO_2 (brown line) (b), Cu/N-TiO_2 (black line) mechanical mixture CuO + N-TiO_2 (red line) (c).

3.2 Photocatalytic activity results

3.2.1 Visible light-driven benzene hydroxylation with Cu/N-TiO_2, Fe/N-TiO_2 and V/N-TiO_2 photocatalysts

It is worth pointing out that N-TiO_2 photocatalyst showed a high benzene conversion (62%) without phenol formation, as already reported in previous studies[18]. Therefore, the visible light-driven benzene oxidation was performed using Cu/N-TiO_2, Fe/N-TiO_2 and V/N-TiO_2 photocatalysts in order to test the possibility of providing higher selectivity towards phenol. The benzene relative concentration and phenol yield as a function of run time with Cu/N-TiO_2, Fe/N-TiO_2 and V/N-TiO_2 photocatalysts are reported in Figure 7.

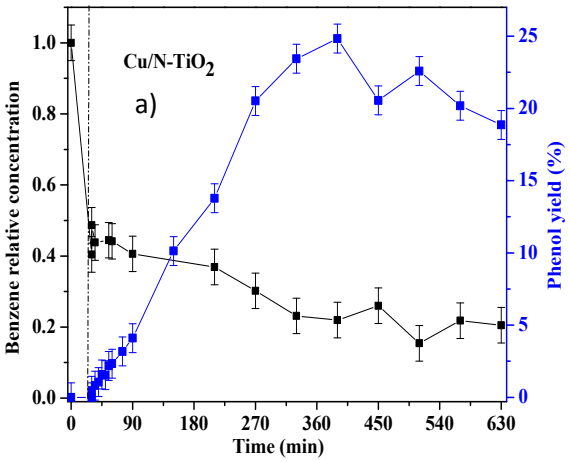

347

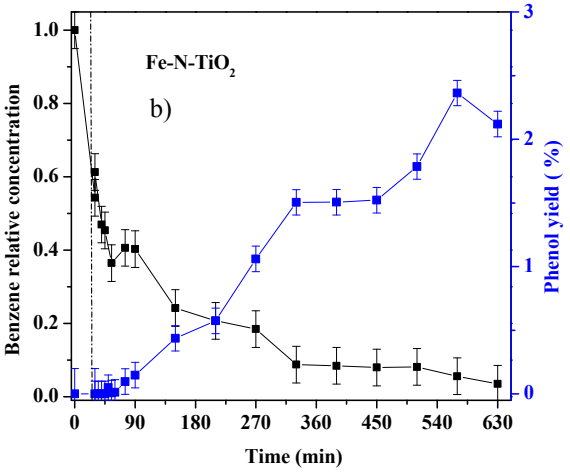

348

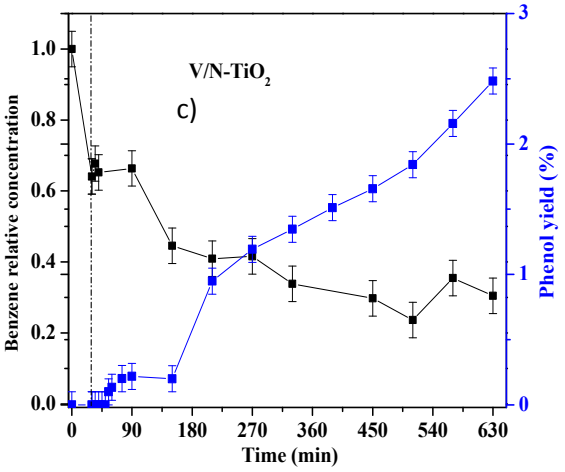

349
350
351
352

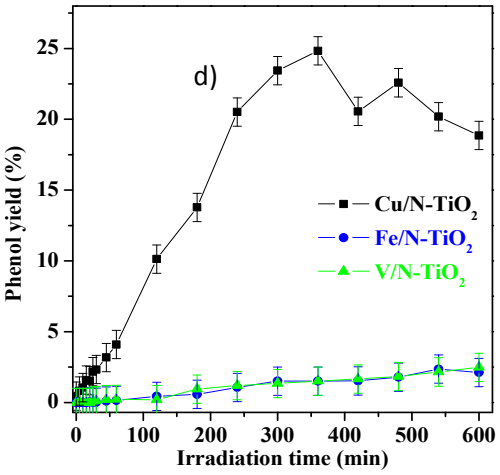

Figure 7. Benzene relative concentration and phenol yield as a function of run time, in dark (up to the dotted line) and under visible light, using Cu/N-TiO_2 (a), Fe/N-TiO_2 (b) and V/N-TiO_2 (c) photocatalysts. Phenol yield as a function of visible irradiation using Cu/N-TiO_2, Fe/N-TiO_2 and V/N-TiO_2 photocatalysts (d).

In the absence of visible light (dark condition), benzene is adsorbed on Cu/N-TiO_2 surface for almost 50% in 30 min (Figure 7a). Despite the presence of H_2O_2 as oxidant, phenol was not produced under dark conditions, indicating that no direct H_2O_2-mediated oxidation occurred. When visible LEDs were switched on, benzene was converted and, consequently, its relative concentration decreased with irradiation time (Figure 7a). Phenol yield gradually increased during irradiation time, reaching a maximum value of 25% after 360 min of irradiation, and then it decreased up to a value of 19% at the end of the test (600 min of visible light). Fe/N-TiO_2 photocatalyst adsorbed benzene for about 46% after 30 min in dark condition (Figure 7b). As the reactor was irradiated with visible LEDs, the reaction has begun, the benzene was converted and the phenol yield was 2% at the end of the test (600 min of visible irradiation). Similarly, V/N-TiO_2 adsorbed benzene in the dark up to 36% (Figure 7c) and, when the photoreaction started, a progressive decrease of benzene relative concentration could be observed providing a phenol yield of about 2.5% after 600 min of irradiation time. For the sake of comparison, Figure 7d shows the phenol yield as a function of irradiation time obtained with Cu/N-TiO_2, Fe/N-TiO_2 and V/N-TiO_2 samples. It is evident that the maximum yield obtained in the presence of the Cu/N-TiO_2 sample (25%) was remarkably higher than that obtained in the presence of the Fe/N-TiO_2 (2%) and V/N-TiO_2 (2.5%) samples.

Table 3 summarizes the values of benzene conversion, and yield and selectivity towards phenol and other oxidation products in the presence of N-TiO_2 alone and coupled with the three considered oxides.

Table 3. Benzene conversion, selectivity to phenol and CO_2 and other ring-opened compounds, yield to phenol, hydroquinone, catechol and resorcinol obtained using N-TiO_2, Cu/N-TiO_2, Fe/N-TiO_2 V/N-TiO_2 powder after 600 min of visible light irradiation.

Catalyst	Bz_{conv}	Y_{phenol}	$Y_{hydroquinone}$	$Y_{catechol}$	$Y_{resorcinol}$	$Y_{p\text{-}benzoquinone}$	S_{phenol}	S_{Deg}
N-TiO_2	62%	n.d	<1%	n.d	n.d	n.d	n.d	>98%
Cu/N-TiO_2	82%	19%	2%	11%	<1%	5%	23%	63%
Fe/N-TiO_2	94%	2%	<1%	n.d	n.d	<1%	2%	97.4%
V/N-TiO_2	71%	2.5%	<1%	<1%	n.d	<1%	3.5%	96.3%

The conversion values obtained in the presence of the three mixed oxides catalytic systems are roughly similar, ranging between 71 and 94%. This agrees with the results of photoluminescence, which show similar suppression of fluorescence for all of the samples, suggesting an efficient spatial charge separation taking place at the interface between the component oxides, as reported in the relevant literature for similar systems[52]. However, phenol selectivity and yield using Cu/N-TiO_2 are higher than those obtained with Fe/N-TiO_2 and V/N-TiO_2 under visible light. The phenol yield achieved with Cu/N-TiO_2 was higher than that observed with TiO_2-based photocatalysts reported in the literature (Table 4). Indeed, under UV light, in most cases the phenol yield was in the range 0.76-16%, lower than that of Cu/N-TiO_2 photocatalyst (25% after 360 min of visible light irradiation). A phenol yield equal to 25.2% was observed on TiO_2 modified with iron and cromium but after 12 h of reaction time and with a benzene conversion (28%)[53] lower that that achieved with Cu/N-TiO_2 (82 % after 600 min of visible light irradiation). It is worth noting to underline that the literature about the visible-light driven hydroxylation of benzene to phenol in presence of TiO_2 based photocatalysts is still scarce.

Table.4 Comparison with literature papers dealing with different photocatalysts for benzene hydroxylation.

Catalyst	Light source	Time of exposure (h)	Photocatalyst dosage (g/L)	Photocatalyst reusability	Benzene conversion (%)	Phenol yield (%)	Ref
$Au/Ti_{0.98}V_{0.02}O_2$	UV	18	6	Not reported	18	15.9	[16]
$Au/Ti_{0.98}V_{0.02}O_2$	visible	18	6	Not reported	-	2	[16]
Fe/TiO_2	UV	4	2.5	Not reported	1.2	1.08	[17]
V/TiO_2	UV	4	2.5	Not reported	0.9	0.76	[17]
Cu/TiO_2	UV	4	2.5	Not reported	1	0.88	[17]
Fe/TiO_2	UV	1-2	10	Not reported	-	9-15	[54]
TiO_2	UV	4	1	Not reported	-	2.6	[14]
Pt/TiO_2	UV	4	1	Not reported	-	2.2	[14]
Pd/TiO_2	UV	4	1	Not reported	-	3.3	[14]
F/TiO_2	UV	4	1	Not reported	-	3.3	[14]
$Fe\text{-}Cr/TiO_2$	UV	12	6	Stable after three reuse cycles	28	25.2	[53]
Fe-V-Cu $/TiO_2$	UV	4	2.5	Not reported	14.3	9.7	[55]
$Cu/N\text{-}TiO_2$	visible	6	0.15	Stable after four reuse cycles	56	25	This work

To explain the higher phenol selectivity and yield achieved with the copper-based photocatalyst, the activity of $Cu/N\text{-}TiO_2$, $Fe/N\text{-}TiO_2$ and $V/N\text{-}TiO_2$ photocatalysts was tested for phenol degradation under visible light as described in the experimental part. Results are reported in Figure 8 along with the adsorption percentage of phenol under dark conditions, for each photocatalytic sample. Notably,

405 as reported in the literature, under the same experimental conditions, N-TiO_2 leads to 77% phenol
406 degradation after 180 min visible light irradiation [56]. However, Figure 8 shows that Fe/N-TiO_2 was
407 the photocatalyst capable of completely degrading phenol. On the contrary, Cu/N-TiO_2 was the less
408 active photocatalyst in the phenol degradation, achieving a very low degradation efficiency of
409 phenol equal to 30% after 180 min of visible light irradiation. A similar trend is apparent as far as
410 the dark adsorption results are concerned. In fact, phenol adsorption under dark conditions is
411 negligible in the presence of Cu/N-TiO_2, while it reaches values of 10 and 20% for V/N-TiO_2 and
412 Fe/N-TiO_2, respectively. By summarizing, while all the three mixed oxides catalytic systems show a
413 similar benzene conversion (Figure 7a, b and c), marked differences among them arise as far as the
414 phenol degradation and dark adsorption are concerned, which follows the order Fe/N-TiO_2 > V/N-
415 TiO_2 > Cu/N-TiO_2 (Figure 8). An opposite trend is observed when considering the selectivity
416 towards phenol, which is, instead, the highest for the Cu/N-TiO_2 photocatalyst. These results can be
417 justified by considering the almost negligible interaction between phenol and the surface of Cu/N-
418 TiO_2 in agreement with the dark adsorption results. Once photocatalytically generated, therefore, the
419 overoxidation of phenol is limited by its favored desorption from the surface of the photocatalyst,
420 thus resulting in its accumulation in the reaction medium. Notably, as often reported for similar
421 photocatalytic systems, also in the case of phenol degradation an inverse relationship between
422 oxidizing capability and selectivity can be observed [57], as a result of the peculiar interaction
423 between a target compound and the surface of the photocatalyst. Therefore, also for the present
424 photocatalytic system, surface phenomena play a key role in determining the selectivity of a
425 photocatalytic reaction [58].

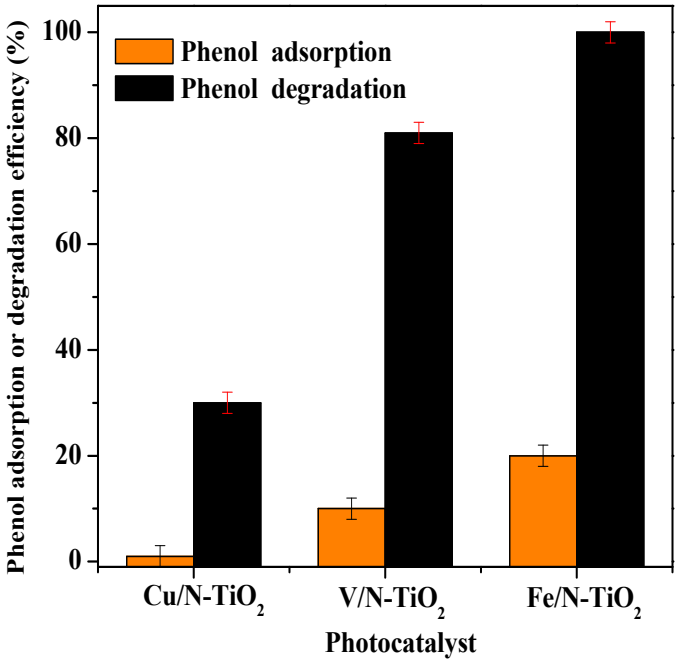

Figure 8. Phenol degradation efficiency after 180 min of visible light irradiation using Cu/N-TiO_2, V/N-TiO_2 and Fe/N-TiO_2 photocatalysts.

The stability trend of Cu/N-TiO_2 photocatalyst was confirmed by performing a series of consecutive photocatalytic oxidation tests in which, after each run, the material was recovered by centrifugation, dried at room temperature for 24 hours and reused in a new catalytic cycle. Based on this procedure, four reuse cycles were carried out under visible LEDs irradiation using the photocatalyst optimized in this work. As shown in Figure 9, no significant decrease in both benzene conversion and phenol

yield was observed in all the reuse cycles, proving the stability of the Cu/N-TiO_2 photocatalyst.

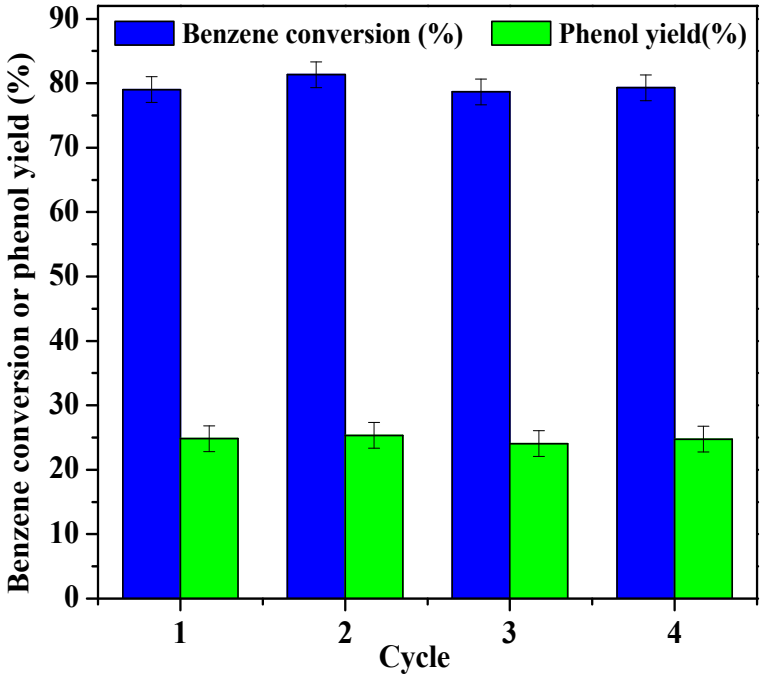

Figure 9. Benzene conversion and phenol yield after 360 min of visible light irradiation for different reuse cycles using Cu/N-TiO_2 photocatalyst.

The WAXD analysis was performed on the Cu/N-TiO_2 recovered from the photoreactor after four reuse cycles (Figure 10).

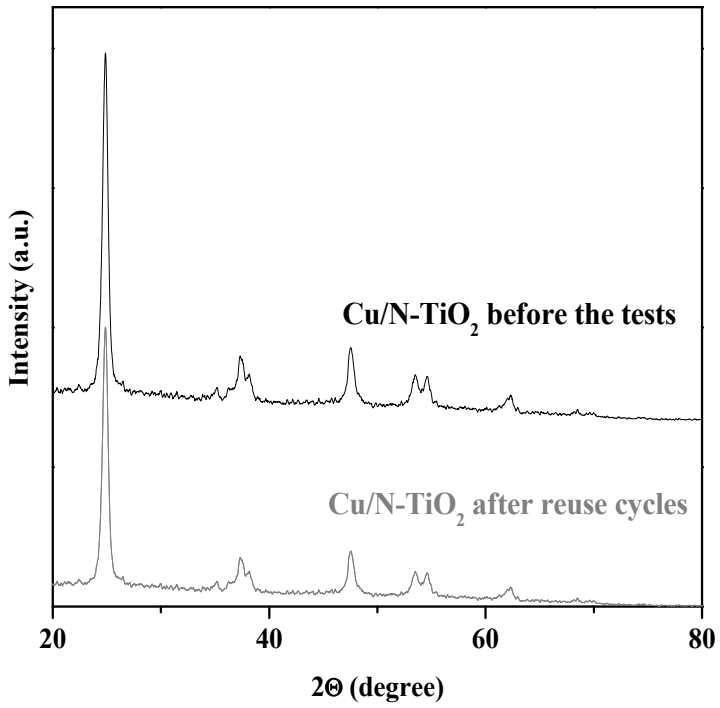

Figure 10. Wide angle X-ray diffraction (WAXD) patterns of Cu/N-TiO_2 before the photocatalytic tests and after four reuse cycles.

No substantial difference with respect to the WAXD spectrum of the catalyst before its use was observed, confirming the stability of Cu/N-TiO_2 photocatalyst in the hydroxylation of benzene.

3.2.3 Kinetic modelling of benzene hydroxylation using Cu/N-TiO_2, Fe/N-TiO_2 and V/N-TiO_2 photocatalysts

The experimental data together with the concentration of by-products detected by HPLC analysis (Figure S3 in Supplementary Material) were used for the kinetic modeling of the three mixed oxide photocatalysts in order to calculate the phenol production kinetic constant for each photocatalytic system.

The main problem of the benzene (BZ) hydroxylation to phenol (PhOH) is related to the consecutive reactions, which lead to by-products such as hydroquinone (HQ), benzoquinone (BQ), catechol (CT), resorcinol (RS) and other ring opening products and eventually CO_2. The identified reaction paths are shown in Figure 11. When the benzene photocatalytic hydroxylation occurs using Cu/N-TiO_2 photocatalyst, the production of all by-products can be observed according to the reaction mechanism shown in Figure 11a. On the other hand, Fe/N-TiO_2 does not provide detectable production of catechol (CT) and resorcinol (RS), suggesting that the route of addition of hydroxyl groups to benzene takes place preferentially in the para position (Figure 11b). Instead, V/N-TiO_2 photocatalyst leads to the production of phenol and the other by-products, except resorcinol (Figure 11c).

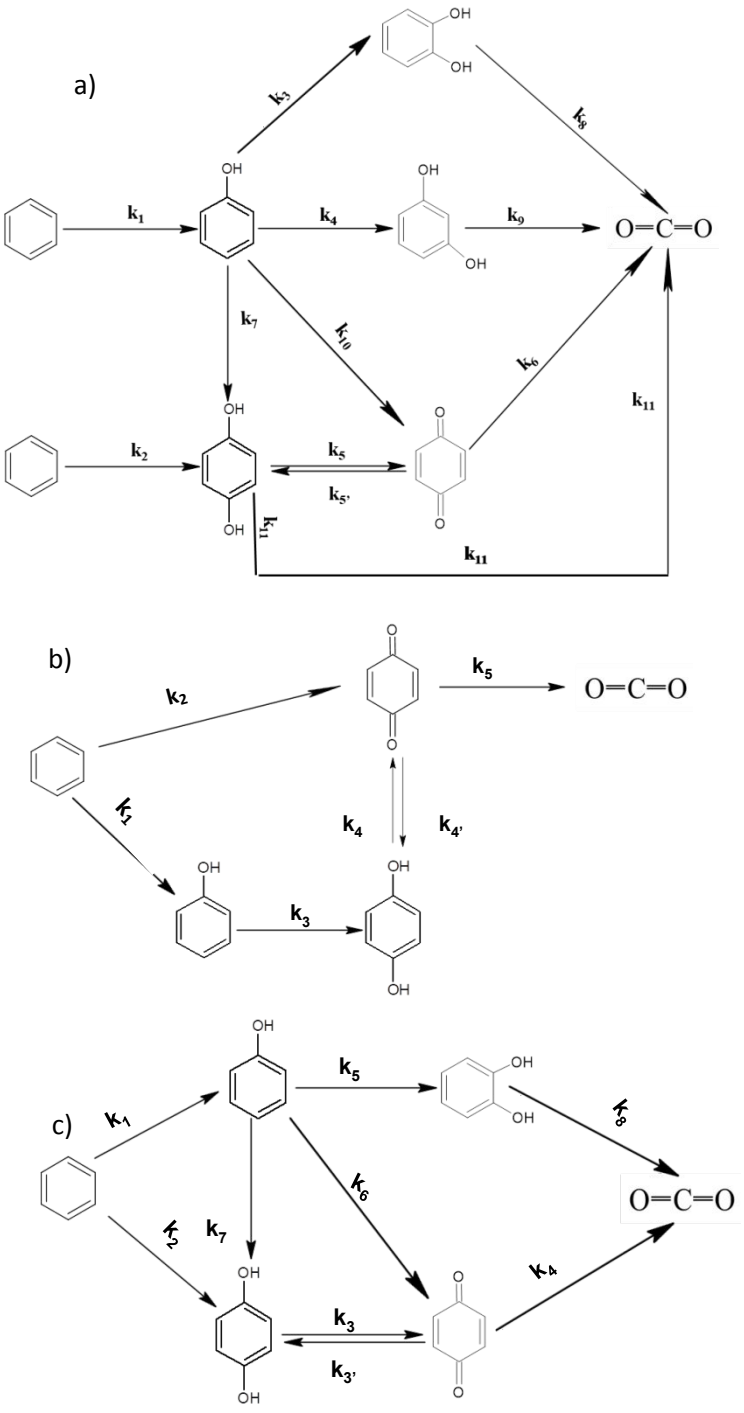

Figure 11. Reaction paths hypothesized for the photocatalytic conversion of benzene with Cu/N-TiO_2 (a), Fe/N-TiO_2 (b) and V/N-TiO_2 (c).

More in detail, under visible light irradiation and in the presence of Cu/N-TiO_2, benzene is directly hydroxylated to phenol and HQ. The oxidative conditions of the system lead to the conversion of HQ to BQ, but the equilibrium reaction between these two species in the aqueous system cannot be excluded, as reported in some literature papers [59]. On the other hand, the production of BQ may occur from phenol, since the •OH radical is highly reactive [59-61]. The concentration of BQ and CA reached appreciable values with respect to the HQ and RS concentration only with the Cu/N-TiO_2 photocatalyst. Therefore, it is hypothesized that CA and RS are produced by phenol hydroxylation (Figure 11a).

Phenol and BQ can be produced by benzene in the presence of irradiated Fe/N-TiO_2, as shown from HPLC analysis (see Supplementary Materials) and consistently with the literature dealing with the oxidation of benzene in presence of copper-based catalysts [62, 63]. HQ can be formed from phenol. Then, HQ is further oxidized to BQ. Also, in this case, the equilibrium reaction between HQ and BQ cannot be excluded (Figure 11b). In the same reaction conditions with V/N-TiO_2 photocatalyst, benzene is directly converted to phenol and HQ that can be further oxidized to BQ. HQ can be produced from benzene and phenol. Consequently, phenol can give CA, HQ and can be directly oxidized to BQ (Figure 11c).

Considering the reaction schemes proposed in Figure 11, a kinetic model for the photocatalytic hydroxylation of benzene is developed, considering first-order kinetics for all the reactions involved in the system [59] [. The mass balance equations for Cu/N-TiO_2 photocatalyst are given below:

$$\frac{dC_{Bz}}{dt} = -k_1 C_{Bz} - k_2 C_{Bz} \quad (4)$$

$$\frac{dC_{PhOH}}{dt} = k_1 C_{Bz} - k_4 C_{PhOH} - k_7 C_{PhOH} - k_3 C_{PhOH} - k_{10} C_{PhOH} \quad (5)$$

$$\frac{dC_{HQ}}{dt} = -k_5 C_{HQ} + k_2 C_{Bz} + k_7 C_{PhOH} + k'_5 C_{BQ} - k_{11} C_{HQ} \quad (6)$$

$$\frac{dC_{CT}}{dt} = k_3 C_{PhOH} - k_8 C_{CT} \quad (7)$$

$$\frac{dC_{RS}}{dt} = k_4 C_{PhOH} - k_9 C_{RS} \quad (8)$$

$$\frac{dC_{BQ}}{dt} = k_5 C_{HQ} - k_6 C_{Bz} - k'_5 C_{Bz} + k_{10} C_{PhOH} \quad (9)$$

$$\frac{dC_{CO_2}}{dt} = 6 * k_6 C_{BQ} + 6 * k_8 C_{CT} + 6 * k_9 C_{RS} + 6 * k_{11} C_{HQ} \quad (10)$$

The mass balance equations for Fe/N-TiO_2 photocatalyst are reported below:

$$\frac{dC_{Bz}}{dt} = -k_1 C_{Bz} - k_2 C_{Bz} \quad (11)$$

$$\frac{dC_{PhOH}}{dt} = k_1 C_{Bz} - k_3 C_{PhOH} \quad (12)$$

$$\frac{dC_{HQ}}{dt} = k_3 C_{PhOH} - k_4 C_{HQ} + k'_4 C_{BQ} \quad (13)$$

$$\frac{dC_{BQ}}{dt} = k_2 C_{BZ} - k_5 C_{BQ} + k_4 C_{HQ} - k'_4 C_{BQ} \quad (14)$$

$$\frac{dC_{CO_2}}{dt} = 6 * k_5 C_{BQ} \quad (15)$$

For V/N-TiO_2 photocatalyst, the mass balance equations are the following:

$$\frac{dC_{Bz}}{dt} = -k_1 C_{Bz} - k_2 C_{Bz} \quad (16)$$

$$\frac{dC_{PhOH}}{dt} = k_1 C_{Bz} - k_5 C_{PhOH} - k_7 C_{PhOH} - k_8 C_{PhOH} \quad (17)$$

$$\frac{dC_{HQ}}{dt} = -k_3 C_{HQ} + k_2 C_{Bz} + k_7 C_{PhOH} + k'_3 C_{BQ} \quad (18)$$

$$\frac{dC_{CT}}{dt} = k_5 C_{PhOH} - k_6 C_{CT} \quad (19)$$

$$\frac{dC_{BQ}}{dt} = k_3 C_{HQ} - k_4 C_{BQ} - k'_3 C_{Bz} + k_8 C_{PhOH} \quad (20)$$

$$\frac{dC_{CO_2}}{dt} = 6 * k_4 C_{BQ} + 6 * k_6 C_{CT} \quad (21)$$

The differential equations for each photocatalyst are solved considering the initial condition:

t=0 $C_{Bz}=C_{BZ_0}$

t=0 $C_{phOH}=C_{HQ}=C_{BQ}=C_{CT}=C_{CO2}=0$

The system of differential equations was solved by a numerical procedure using the Euler method. It is the most basic explicit method for the numerical integration of ordinary differential equations (ODEs) with a given initial value. The values of the apparent kinetic constant for each reaction were attained by using the least-squares approach, minimizing the sum of squared residuals between the experimental data acquired at different irradiation times and the values provided by the model. The comparison between the model and experimental results is reported in Figure 12.

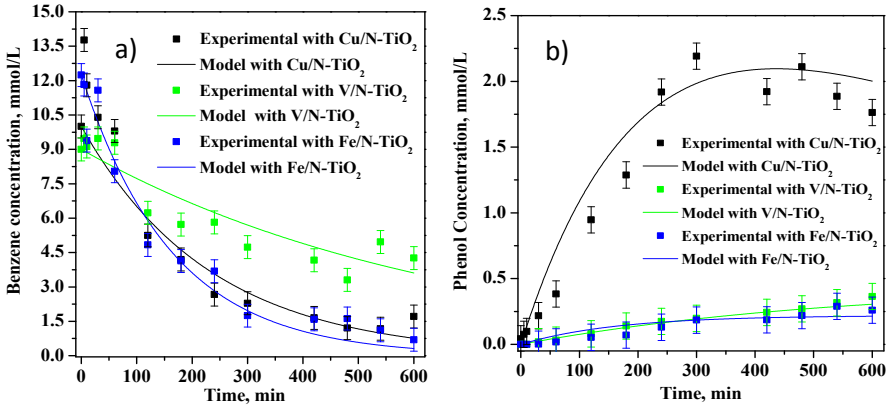

Figure 12. Comparison between model calculation and experimental data to find the model oxidation constant k for benzene concentration (mmol/L) (a); phenol concentration (mmol/L) as a function of time obtained with Cu/N-TiO_2, Fe/N-TiO_2 and V/N-TiO_2 under visible light (b).

Table 5 shows the kinetic constants for phenol production (k_1).

Table 5. Phenol production kinetic constants (k_1) derived from the proposed mechanism for photocatalytic hydroxylation of benzene considering Cu/N-TiO_2, Fe/N-TiO_2 and V/N-TiO_2 samples.

Photocatalyst	k_1 (min^{-1})
Cu/N-TiO_2	$1.41 \cdot 10^{-3}$
Fe/N-TiO_2	$1.09 \cdot 10^{-4}$
V/N-TiO_2	$9.21 \cdot 10^{-5}$

The values of the phenol production kinetic constants evidenced that the Cu/N-TiO_2 photocatalyst showed the highest rate of phenol formation with respect to the other formulated photocatalysts. Ultimately, Cu/N-TiO_2 photocatalyst is more effective as it produces phenol faster than the other formulated photocatalysts and it allows achieving the highest phenol yield (19%) and selectivity to phenol (23%) after 600 min of visible light irradiation.

Considering the mechanisms reported in the available literature [53, 64-66], it is possible to argue that the oxidation of benzene to phenol on Cu/N-TiO_2 may occur through the following reactions:

$$N\text{-}TiO_2 + h\nu \longrightarrow e_{CB}^- + h^+ \quad (22)$$

$$Cu^{2+} + e_{CB}^- \longrightarrow Cu^+ \quad (23)$$

$$Cu^+ + H_2O_2 \longrightarrow Cu^{2+} + \bullet OH + OH^- \quad (24)$$

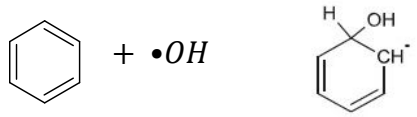
(25)

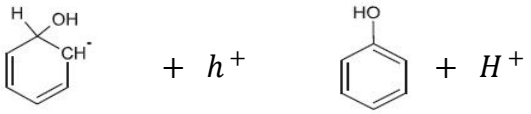
(26)

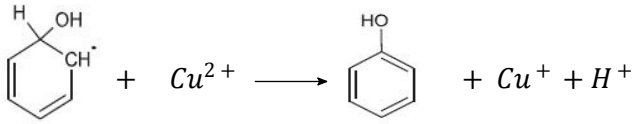
(27)

The hole-electron pairs are produced from the activation of the transition metal oxides or N-TiO_2 (Eq. 22) under irradiation. Cupric ions could react with the photogenerated electrons, producing cuprous ions (Eq. 23). Therefore, Cu^+ ions could be re-oxidized to Cu^{2+} by H_2O_2, generating •OH (Eq. 24). The hydroxyl radical reacts with benzene to generate hydroxylated benzene radical (Eq. 25), which is then oxidized by a positive hole (Eq. 25) or by Cu^{2+} (Eq. 26) on the photocatalyst surface and deprotonated, eventually producing phenol.

4. Conclusions

Transition metal oxides supported on N-TiO_2 (Cu/N-TiO_2, Fe/N-TiO_2, and V/N-TiO_2) were synthesized by incipient wet impregnation and their physico-chemical properties were studied by means of different characterization techniques. Wide-angle X-ray diffraction patterns and Raman spectra showed the presence of signals typical of the anatase crystalline phase for all of the

synthesized samples. In the diffraction pattern of Cu/N-TiO_2 additional peak related to CuO phase was observed. Additionally, from Raman analysis of V/N-TiO_2 sample, bands assigned to the presence of polyvanadates dispersed on the surface were detected. Fluorescence spectra indicated an efficient suppression of the charge recombination for all of the mixed oxide catalytic systems. However, UV-vis spectra evidenced significant electronic interactions between N-TiO_2 and the copper oxide, resulting in a remarkable red shift of the absorption edge for the Cu/N-TiO_2 with respect to the Fe/N-TiO_2, and V/N-TiO_2 samples. The obtained mixed oxide photocatalytic systems were employed for the benzene to phenol conversion reaction in presence of H_2O_2 and under visible light. N-TiO_2 showed high benzene conversion (62%) without phenol formation under visible light. A maximum yield towards phenol of ca. 25% was achieved in the presence of Cu/N-TiO_2, significantly higher than that observed with Fe/N-TiO_2 (2%) and V/N-TiO_2 (2.5%). Cu/N-TiO_2 photocatalyst is more effective as it produces phenol faster than the other formulated photocatalysts and it allows achieving phenol in a selective way (after 600 min, selectivity of 23% with high benzene conversion of 82%). The superior performance of the Cu/N-TiO_2 sample can be ascribed partially to the better optical absorption but especially to the low affinity of phenol with the copper oxide component. Indeed, the photocatalytic degradation of phenol was the slowest in the presence of Cu/N-TiO_2 photocatalyst, which, on the other hand, showed the highest performance in the hydroxylation of benzene to phenol compared to Fe/N-TiO_2 and V/N-TiO_2. Finally, Cu/N-TiO_2 proved to be a very stable catalytic material as any significant decrease both in the conversion of benzene and in the phenol yield after four cycles of reuse was evidenced. Based on the results achieved in this work, for the possible industrialization of a catalytic reactor devoted to the hydroxylation of benzene to phenol in the liquid phase, it is necessary to develop a fixed-bed

photoreactor in which a structured catalyst, realized through the immobilization of Cu/N-TiO_2 photocatalyst on a macroscopic support, is placed. This could prevent a further separation step of the catalytic powders from the liquid medium at the end of the oxidation phase. Moreover, it could be affordable to design efficient and low-cost systems for separating and recovering phenol from the liquid phase, as reported for similar partial oxidation reactions[67].

References

1. V. Zakoshansky, *Petroleum Chemistry*, 2007, **47**, 273-284.
2. J. Fortuin and H. Waterman, *Chemical Engineering Science*, 1953, **2**, 182-192.
3. A. Mancuso, O. Sacco, D. Sannino, V. Venditto and V. Vaiano, *Catalysts*, 2020, **10**, 1424.
4. N. Rahmani, A. Amiri, G. M. Ziarani and A. Badiei, *Molecular Catalysis*, 2021, **515**, 111873.
5. F. R. Pomilla, E. García-López, G. Marcì, L. Palmisano and F. Parrino, *Materials Today Sustainability*, 2021, **13**, 100071.
6. R. Koutavarapu, K. Syed, S. Pagidi, M. Y. Jeon, M. Rao, D.-Y. Lee and J. Shim, *Chemosphere*, 2022, **287**, 132015.
7. Z. Zheng, F. Han, B. Xing, X. Han and B. Li, *Journal of Colloid and Interface Science*, 2022, **624**, 460-470.
8. F. Parrino, M. D'Arienzo, S. Mostoni, S. Dirè, R. Ceccato, M. Bellardita and L. Palmisano, *Topics in Current Chemistry*, 2022, **380**, 1-15.
9. C. Lefebvre and N. Hoffmann, in *Nontraditional Activation Methods in Green and Sustainable Applications*, Elsevier, 2021, pp. 283-328.
10. M. H. Shaw, J. Twilton and D. W. MacMillan, *The Journal of organic chemistry*, 2016, **81**, 6898-6926.
11. J. Kou, C. Lu, J. Wang, Y. Chen, Z. Xu and R. S. Varma, *Chemical reviews*, 2017, **117**, 1445-1514.
12. R. Molinari, P. Argurio and T. Poerio, *Industrial & Engineering Chemistry Research*, 2013, **52**, 10540-10548.
13. G. Camera-Roda, V. Loddo, L. Palmisano, F. Parrino and F. Santarelli, *Chemical Engineering Journal*, 2017, **310**, 352-359.
14. H. Park and W. Choi, *Catalysis Today*, 2005, **101**, 291-297.
15. Y. Ide, M. Matsuoka and M. Ogawa, *Journal of the American Chemical Society*, 2010, **132**, 16762-16764.
16. P. Devaraji, N. K. Sathu and C. S. Gopinath, *Acs Catalysis*, 2014, **4**, 2844-2853.
17. G. Tanarungsun, W. Kiatkittipong, S. Assabumrungrat, H. Yamada, T. Tagawa and P. Praserthdam, *Journal of Chemical Engineering of Japan*, 2007, **40**, 415-421.

18. A. Mancuso, V. Vaiano, P. Antico, O. Sacco and V. Venditto, *Catalysis Today*, 2023, **413**, 113914.
19. O. Sacco, M. Stoller, V. Vaiano, P. Ciambelli, A. Chianese and D. Sannino, *International Journal of Photoenergy*, 2012, **2012**.
20. J. Papp, S. Soled, K. Dwight and A. Wold, *Chemistry of materials*, 1994, **6**, 496-500.
21. F. T. L. Muniz, M. R. Miranda, C. Morilla dos Santos and J. M. Sasaki, *Acta Crystallographica Section A: Foundations and Advances*, 2016, **72**, 385-390.
22. O. Sacco, A. Mancuso, V. Venditto, S. Pragliola and V. Vaiano, *Catalysts*, 2022, **12**, 1208.
23. W. Navarra, I. Ritacco, O. Sacco, L. Caporaso, M. Farnesi Camellone, V. Venditto and V. Vaiano, *The Journal of Physical Chemistry C*, 2022, **126**, 7000-7011.
24. G. Zhang, J. Yi, J. Shim, J. Lee and W. Choi, *Applied Catalysis B: Environmental*, 2011, **102**, 132-139.
25. T. Theivasanthi and M. Alagar, *arXiv preprint arXiv:1307.1091*, 2013.
26. L. Gnanasekaran, R. Pachaiappan, P. S. Kumar, T. K. Hoang, S. Rajendran, D. Durgalakshmi, M. Soto-Moscoso, L. Cornejo-Ponce and F. Gracia, *Environmental Pollution*, 2021, **287**, 117304.
27. L. Rizzo, D. Sannino, V. Vaiano, O. Sacco, A. Scarpa and D. Pietrogiacomi, *Applied Catalysis B: Environmental*, 2014, **144**, 369-378.
28. G.-H. Lee, M. S. Lee, G.-D. Lee, Y.-H. Kim and S.-S. Hong, *Journal of Industrial and Engineering Chemistry*, 2002, **8**, 572-577.
29. P. Magesan, P. Ganesan and M. Umapathy, *Optik*, 2016, **127**, 5171-5180.
30. M. Giarola, A. Sanson, F. Monti, G. Mariotto, M. Bettinelli, A. Speghini and G. Salviulo, *Physical Review B*, 2010, **81**, 174305.
31. G. Vitiello, L. Clarizia, W. Abdelraheem, S. Esposito, B. Bonelli, N. Ditaranto, A. Vergara, M. Nadagouda, D. D. Dionysiou and R. Andreozzi, *ChemCatChem*, 2019, **11**, 4314-4326.
32. P. Panta and C. Bergmann, *J. Mater. Sci. Eng*, 2015, **5**.
33. P. Ciambelli, D. Sannino, V. Palma, V. Vaiano and R. Mazzei, *Photochemical & Photobiological Sciences*, 2009, **8**, 699-704.
34. N. X. r. P. S. Database, 2000.
35. G. Silversmit, D. Depla, H. Poelman, G. B. Marin and R. De Gryse, *Journal of Electron Spectroscopy and Related Phenomena*, 2004, **135**, 167-175.
36. Z. Ambrus, N. Balázs, T. Alapi, G. Wittmann, P. Sipos, A. Dombi and K. Mogyorósi, *Applied Catalysis B: Environmental*, 2008, **81**, 27-37.
37. É. G. Bajnóczi, N. Balázs, K. Mogyorósi, D. F. Srankó, Z. Pap, Z. Ambrus, S. E. Canton, K. Norén, E. Kuzmann and A. Vértes, *Applied Catalysis B: Environmental*, 2011, **103**, 232-239.
38. N. D. Abazović, M. I. Čomor, M. D. Dramićanin, D. J. Jovanović, S. P. Ahrenkiel and J. M. Nedeljković, *The Journal of Physical Chemistry B*, 2006, **110**, 25366-25370.
39. S. Abdullah, M. Sahdan, N. Nafarizal, H. Saim, A. Bakri, C. Rohaida, F. Adriyanto and Y. Sari, 2018.
40. M. Rajabi and S. Shogh, *Journal of Luminescence*, 2015, **157**, 235-242.
41. W. Hu, F. Dong, J. Zhang, M. Liu, H. He, D. Yang and H. Deng, *Research on Chemical Intermediates*, 2018, **44**, 705-720.
42. C. Wei, Z. Peng, P. Zhang and J. Duan, 2018.

43. H. Tang, K. Prasad, R. Sanjines, P. Schmid and F. Levy, *Journal of applied physics*, 1994, **75**, 2042-2047.
44. K. Selvam, S. Balachandran, R. Velmurugan and M. Swaminathan, *Applied Catalysis A: General*, 2012, **413**, 213-222.
45. S. Zhang, X. Gong, Q. Shi, G. Ping, H. Xu, A. Waleed and G. Li, *ACS omega*, 2020, **5**, 15942-15948.
46. M. Dhonde, K. S. Dhonde and V. Murty, *Journal of Materials Science: Materials in Electronics*, 2018, **29**, 18465-18475.
47. K. M. Reddy, S. V. Manorama and A. R. Reddy, *Materials Chemistry and Physics*, 2003, **78**, 239-245.
48. P. Ji, M. Takeuchi, T.-M. Cuong, J. Zhang, M. Matsuoka and M. Anpo, *Research on Chemical Intermediates*, 2010, **36**, 327-347.
49. K. Maeda and K. Domen, *The journal of physical chemistry C*, 2007, **111**, 7851-7861.
50. H. Lachheb, F. Ajala, A. Hamrouni, A. Houas, F. Parrino and L. Palmisano, *Catalysis Science & Technology*, 2017, **7**, 4041-4047.
51. H. Tada, Q. Jin, H. Nishijima, H. Yamamoto, M. Fujishima, S. i. Okuoka, T. Hattori, Y. Sumida and H. Kobayashi, *Angewandte Chemie International Edition*, 2011, **15**, 3501-3505.
52. A. Hamrouni, H. Azzouzi, A. Rayes, L. Palmisano, R. Ceccato and F. Parrino, *Nanomaterials*, 2020, **10**, 795.
53. P. Devaraji and W.-K. Jo, *Applied Catalysis A: General*, 2018, **565**, 1-12.
54. N. Gupta, P. Bansal and B. Pal, *Journal of Experimental Nanoscience*, 2015, **10**, 148-160.
55. G. Tanarungsun, W. Kiatkittipong, S. Assabumrungrat, H. Yamada, T. Tagawa and P. Praserthdam, *Journal of Industrial and Engineering Chemistry*, 2007, **13**, 870-877.
56. V. Vaiano, O. Sacco, D. Sannino, M. Stoller, P. Ciambelli and A. Chianese, *Chemical Engineering Transactions*, 2016, **47**, 235-240.
57. A. Gottuso, A. Köckritz, M. L. Saladino, F. Armetta, C. De Pasquale, G. Nasillo and F. Parrino, *Journal of Catalysis*, 2020, **391**, 202-211.
58. F. Parrino, C. De Pasquale and L. Palmisano, *ChemSusChem*, 2019, **12**, 589-602.
59. B. C. Salgado and A. Valentini, *Brazilian Journal of Chemical Engineering*, 2020, **36**, 1501-1518.
60. E. V. Rokhina and J. Virkutyte, *Critical Reviews in Environmental Science and Technology*, 2010, **41**, 125-167.
61. K. Parida and D. Rath, *Applied Catalysis A: General*, 2007, **321**, 101-108.
62. W. H. Wanna, R. Ramu, D. Janmanchi, Y.-F. Tsai, N. Thiyagarajan and S. S.-F. Yu, *Journal of Catalysis*, 2019, **370**, 332-346.
63. C. Li, Q. Zhang and A. Zeng, *Transactions of Tianjin University*, 2019, **25**, 517-526.
64. O. Tomita, R. Abe and B. Ohtani, *Chemistry Letters*, 2011, **40**, 1405-1407.
65. V. D. Dasireddy and B. Likozar, *Journal of the Taiwan Institute of Chemical Engineers*, 2018, **82**, 331-341.
66. M. Janczarek and E. Kowalska, *Catalysts*, 2017, **7**, 317.
67. G. Camera-Roda, A. Cardillo, V. Loddo, L. Palmisano and F. Parrino, *Membranes*, 2014, **4**, 96-112.

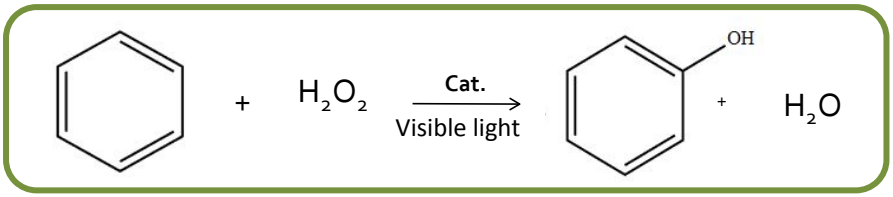
OH
+
H_2O_2
Cat.
Visible light
+
H_2O

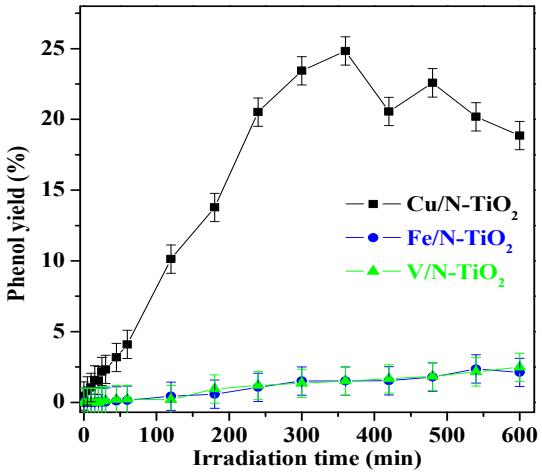
Phenol yield (%)
Irradiation time (min)
Cu/N-TiO2
Fe/N-TiO2
V/N-TiO2

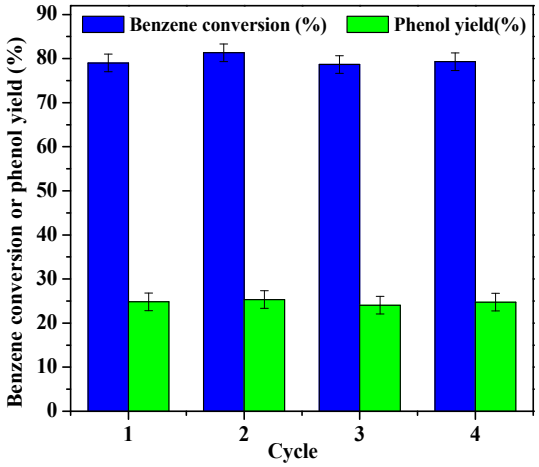
Benzene conversion (%)
Phenol yield(%)
Benzene conversion or phenol yield (%)
Cycle

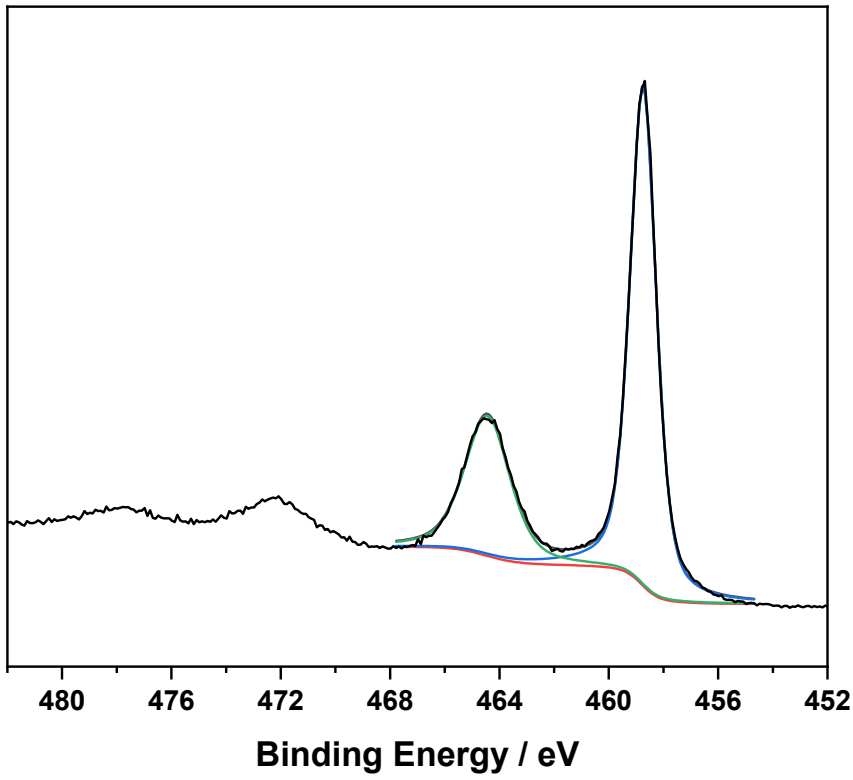

Figure S1. Ti2p region for N-TiO_2 samples.

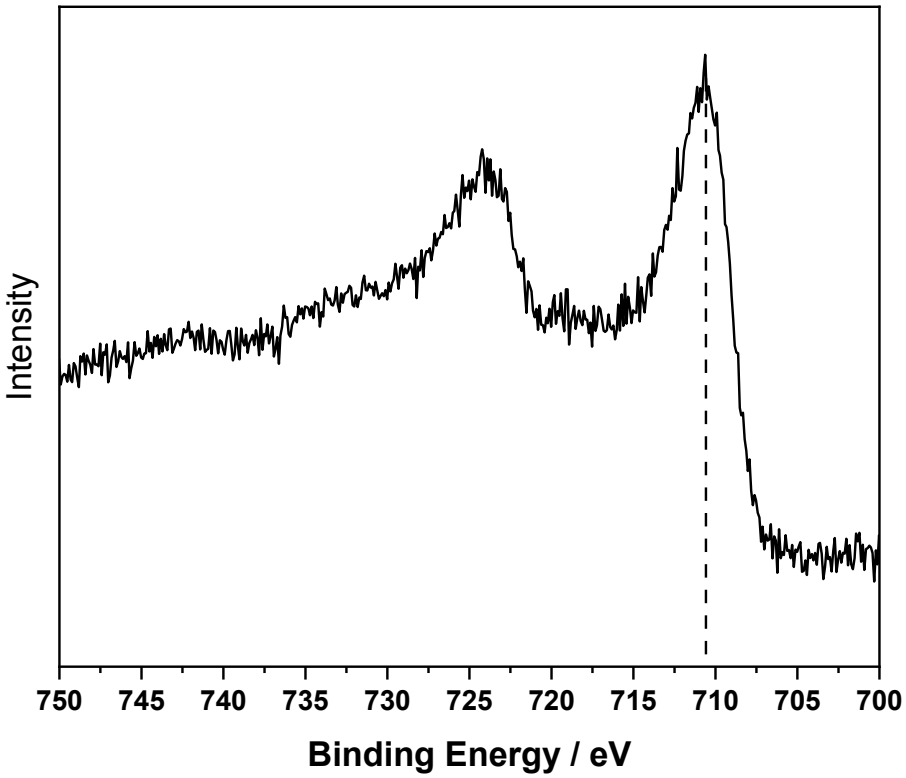

Figure S2. Fe2p region for Fe/N-TiO_2 samples. Average maximum position for $Fe2p_{3/2}$ is indicated by a dashed line.

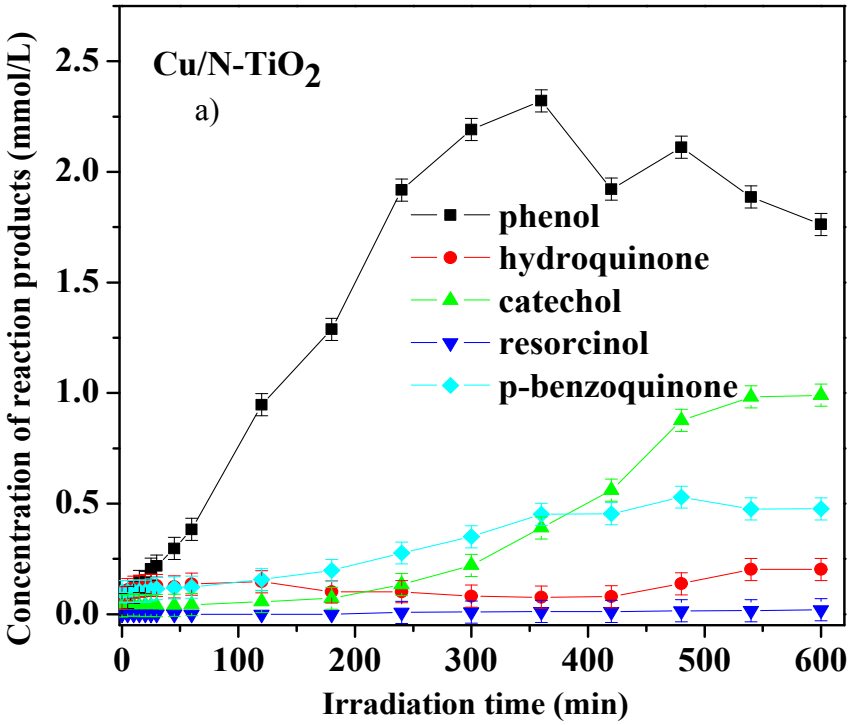
Cu/N-TiO2
a)
phenol
hydroquinone
catechol
resorcinol
p-benzoquinone
Concentration of reaction products (mmol/L)
Irradiation time (min)
0.0
0.5
1.0
1.5
2.0
2.5
0
100
200
300
400
500
600

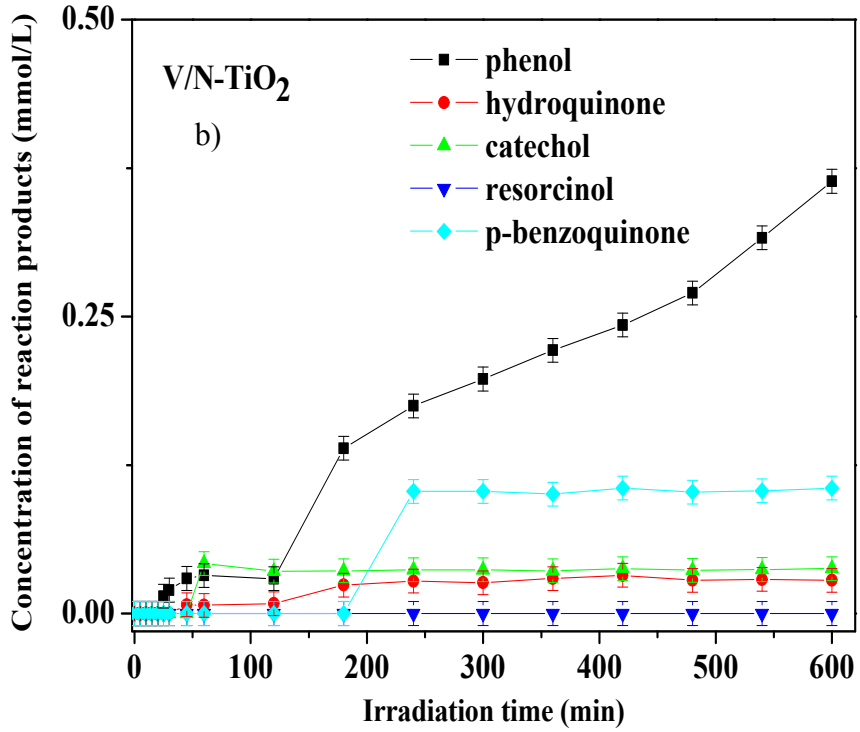
V/N-TiO2
b)
phenol
hydroquinone
catechol
resorcinol
p-benzoquinone
Concentration of reaction products (mmol/L)
Irradiation time (min)
0.00
0.25
0.50
0
100
200
300
400
500
600

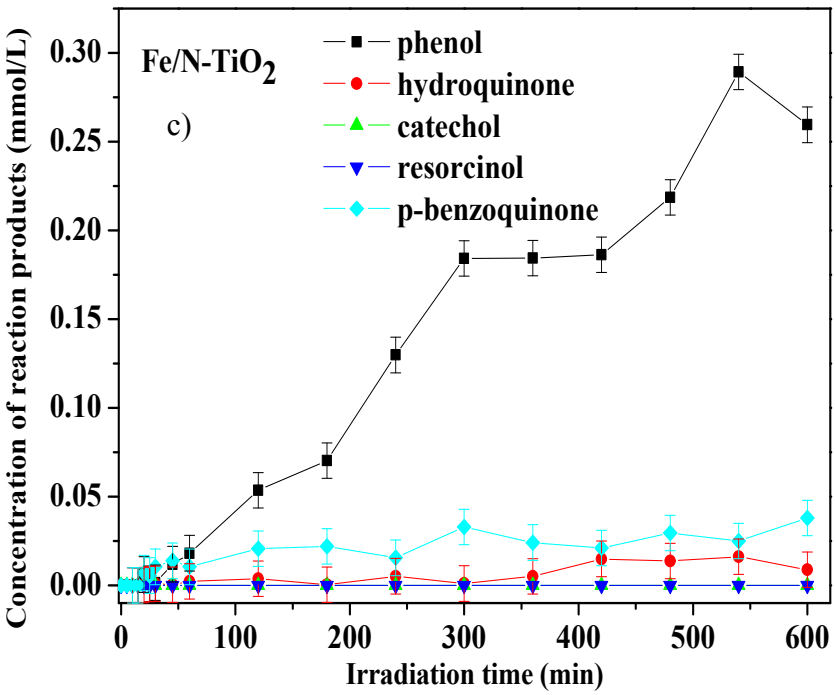

Figure S3. a) Reaction products concentration (mmol/L) as function of irradiation time (min) with Cu/ N-TiO_2 photocatalyst under visible light irradiation; b) Reaction products concentration (mmol/L) as function of irradiation time (min) with V/ N-TiO_2 photocatalyst under visible light irradiation c)Reaction products concentration (mmol/L) as function of irradiation time (min) with Fe/ N-TiO_2 photocatalyst under visible light irradiation.